Science Advances
AAAS

Supplementary Materials for

Spontaneous snapping-induced jet flows for fast, maneuverable surface and underwater soft flapping swimmer

Haitao Qing *et al.*

Corresponding author: Jie Yin, jyin8@ncsu.edu

Sci. Adv. **10**, eadq4222 (2024)
DOI: 10.1126/sciadv.adq4222

The PDF file includes:

Other Supplementary Material for this manuscript includes the following:

Supplementary Text

Rotation and flapping performance of the soft flapping swimmer

The phenomenon of snapping is known to significantly amplify both rotation and flapping motions of prestressed wings by rapidly releasing its prestored strain energy. This effect is particularly prominent in soft-bodied organisms, requiring only minimal 2D bending deformation and low actuation energy. To explore the relationship between pneumatic actuation-induced 2D bending deformation in soft bodies and the resulting amplified 3D flapping behavior in prestressed wings, the following parameters are tracked. Specifically, we tracked the rotation angle φ_{wing} with respect to the bending angle φ_{body} (**Fig. S12a**) and the flapping angle θ_{wing} with respect to deflection d_{body} (**Fig. S12b**). **Fig. S12c** shows the definitions of all the angles and deflections of soft body and prestressed wing. During the snap-through motion, the bending angle of the soft body increases around 5°, resulting in a large rotating change in the wing of approximately 120°. Equivalently, the deflection of the soft body only increases about 4 mm, whereas the flapping angle of the prestressed wing changes by about 20°. For the snap-back motion, the soft body and prestressed wing show a similar trend to the snap-through motion. Compared to the deformation before snapping motions, snapping amplifies the rotation and flapping of the prestressed wing only with a small deformation of the soft body under the one air inflation, which benefits the high-speed swimming. **Fig. S12d** shows the relationship between angular velocity ω and time. Compared to the small value of the angular velocity of the soft body during one cycle, the prestressed wing shows two peaks in a very short time. One corresponds to the snap-through motion, and the other one corresponds to the snap-back motion. The soft body triggers ultrafast snapping motions, which are hundreds of times larger than its angular velocity (**Fig. S12d**). The relationship between the flapping angle of the wing and the difference values of deflection of the soft body shows the snap-through and snap-back can trigger a large flapping motion of the wing in a very short time (**Fig. S12e**).

Setup for the particle image velocimetry tests

The flow field measurements were conducted in the recirculating water tunnel facility at the University of Virginia. A rendering of the experimental setup is shown in **Fig. S18a**, followed by a side view (**Fig. S18b**) and a rear view (**Fig. S18c**). The water tunnel test section has a dimension of W×H×L=0.38 m×0.45 m×1.52 m. In the experiments, the flow velocity was kept constant at

U=0.1 m/s, monitored by an ultrasonic flow meter (Dynasonics Series TFXB), resulting in a chord-based Reynolds number Re=ρUc⁄μ=6550, where ρ and μ are water density and viscosity, respectively. The soft flapping actuator was mounted horizontally in the water flow, supported by a plastic holder that extended out from the water surface. A baffle plate was added to the water-air interface to eliminate any free surface effects.

Planar particle image velocimetry (PIV) was used to measure the velocity vectors around the soft flapping actuator and in the wake at two spanwise locations – the middle point and the quarter point. The flow was seeded using neurally buoyant silver-coated hollow ceramic particles (Potters Industries) which have an average diameter of 50 m. Two vertical laser sheets, one above the water tunnel and one below the tunnel, were used to illuminate the particles. The laser sheets were generated by two continuous wave lasers (532 nm, 5W Raypower MGL-W-532 and 10W CNI MGL-W-532A) with sheet optics. A high-speed camera (Phantom SpeedSense M341, 2560×1600 pixels) perpendicular to the laser sheet was used to record the PIV image pairs at a frequency of 50 Hz. Another high-speed camera was used to track the instantaneous motion of the soft actuator for 3D shape reconstruction. The PIV raw images were fed into the Dantec Dynamic Studio (v6.9) software for velocity vector calculation. The software utilized an adaptive PIV algorithm with a minimum interrogation window size of 3232 pixels and a maximum window size of 6464 pixels. For each spanwise location, 1000 consecutive velocity vector fields were obtained. These velocity fields were divided into 40 bins based on their phase. In each bin, 25 velocity fields were phase-averaged to eliminate instantaneous variations of the flow structures while maintaining the most coherent features across different motion cycles. The flow structures around the soft flapping actuator and in the wake were visualized by the spanwise vorticity, calculated as =dv/dx-du/dy, where u and v are velocities in the x and y direction, respectively. **Fig. S18d** shows the vorticity field before and after the snap through (around 220 ms) and snap back (around 700 ms), with red regions representing positive, counterclockwise vorticities, and blue regions representing negative, clockwise vorticities.

Setup for the computational fluid dynamics

To analyze the 3D vortex and wake formation of the snapping robot, an immersed-boundary method (IBM) direction numerical simulation (DNS) is conducted. Using video recordings of the

experiments shown in **Fig. S19**, the body geometry and flapping kinematics of the specimen are reconstructed for flow simulation. A point-based reconstruction method is used, as shown in **Fig. S19 (a)**. White dots are applied uniformly to the fin surface of the specimen, as shown in **Fig. S19 (a1)**. Then a template computational surface mesh is constructed and overlaid onto the video recording, with surface nodes matching the pixel locations of the white dots, as shown in **Fig. S19 (a2)**. A typical cycle of snapping motion, complete with the snap-through and the snap-back, beginning and ending with the same fin deformation, was used to reconstruct the deformation kinematics. At regular intervals of the video recording, key frames are chosen to apply the process shown in **Fig. S19 (a2)**, where the surface nodes are moved to the pixel locations of the white dot. This method of reconstructing deformation kinematics is based on the method used by Koehler et al. to produce accurate surface deformation of a dragonfly wing *(57)*. After the reconstruction of the kinematics using the template surface mesh, it is then subdivided, smoothed and triangulated using the Catmull-Clark subdivision method to produce the dense, uniform and high-isotropy surface mesh shown in **Fig. S19 (a2)**.

The flow around the model shown in **Fig. S19 (a2)** with kinematics reconstructed from PIV experiments was then simulated on a Cartesian spatial grid as shown in **Fig. S19 (b)**. The DNS solver solves the Navier-Stokes equations using a finite-difference method. The algorithm and details of the flow solver is outlined in *(58)* and *(59)*. A tree-topological local mesh refinement (TLMR) *(59)* is used to achieve high resolution of flow features near the immersed boundary and its immediate wake, while also maintaining low computational cost. A smaller TLMR block (block 1) subdividing the background grid (block 0) spacing by half is applied surrounding the immersed boundary and its wake.

Underwater swimming behaviors of soft flapping swimmers with different attached weights

We investigate the use of attached weights on soft flapping swimmers for underwater swimming. As schematically illustrated in **Fig. S21a**, a sphere weight is attached to the belly of the soft body to enable underwater swimming, while ensuring that it does not interfere with the snapping behavior. The analog control scheme for the output driving signal from the control circuit is depicted in **Fig. S21b**. In this scheme, the pulsed amplitude and time for the driving voltage are fixed at 12-Vpp and 200 ms, respectively, while the time intervals between two voltage pulses are

fixed at 600 ms. The overlapping time-lapse images of swimming behaviors for soft flapping swimmers with different attached sphere weights under the same actuation frequency of f = 1.25 Hz are shown in **Fig. S21c-e**. When the sphere weight is set to 0.38 g, the soft flapping swimmer can initiate swimming from the water bottom and rapidly ascend to the air-water interface in a slanted manner. It then continues swimming forward at the air-water interface (**Fig. S21c**). Similarly, when the sphere weight is set to 0.68 g, the soft flapping swimmer also starts swimming from the water bottom and gradually ascends underwater in a gentle slope (**Fig. S21d**). Notably, with a sphere weight of 1.4 g, the soft flapping swimmer is capable of swimming at the water bottom (**Fig. S21e**). The soft flapping swimmer generates a wave-like undulation to swim forward, as shown in the time-lapse tracked trajectories in X direction of its soft body mass center in **Fig. S21f**.

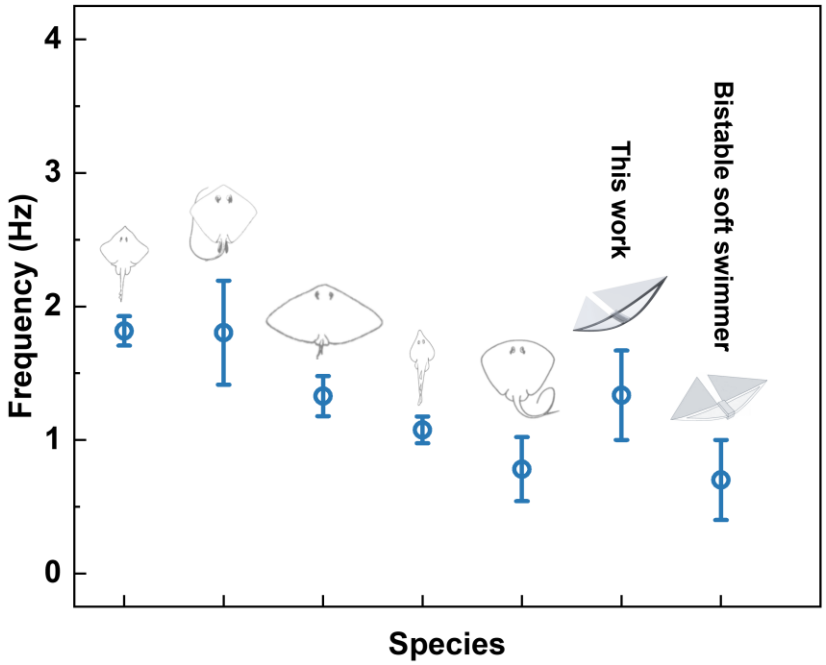

Fig. S1. Comparison of frequencies of this work with bistable soft swimmer and batoids. Clearnose skate (1.63 – 1.93 Hz); Southern stingray (1.34 – 2.19 Hz); Smooth butterfly ray (1.14 – 1.48 Hz); Guitarfish (0.89 – 1.17 Hz); Pelagic stingray (0.51 – 1.02 Hz); Bistable soft swimmer (0.4 – 1 Hz); This work (1 – 1.67 Hz) *(6)*.

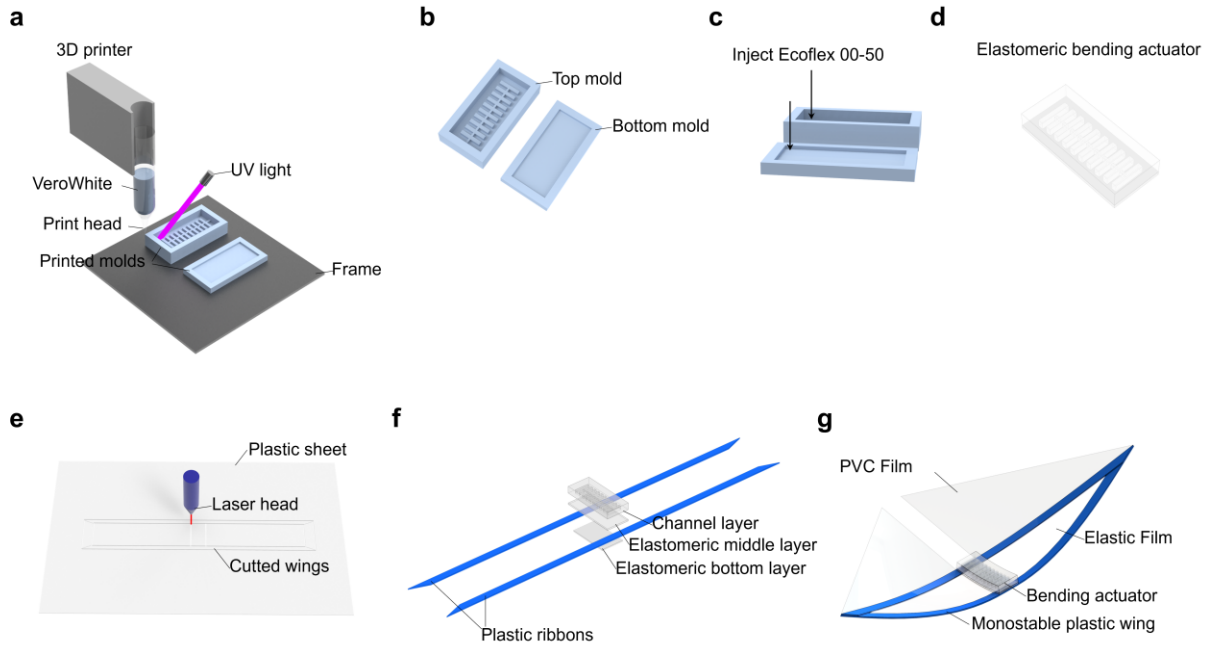

Fig. S2. Fabrication process of the soft flapping swimmer. (a) 3D printing of molds. (b) Top mold and bottom molds for the elastomer curing process. (c) Elastomer curing process. (d) Assembled elastomeric bending actuator. (e) Laser cutting of polyester ribbons. (f) Assembly of five components, including two polyester ribbons, one of elastomeric channel layer, and elastomeric middle and bottom layers. (g) Bonding two pairs of tips of polyester ribbons to form the soft flapping swimmer, after attaching the PVC film as the tail fins and the elastic film for wing covering.

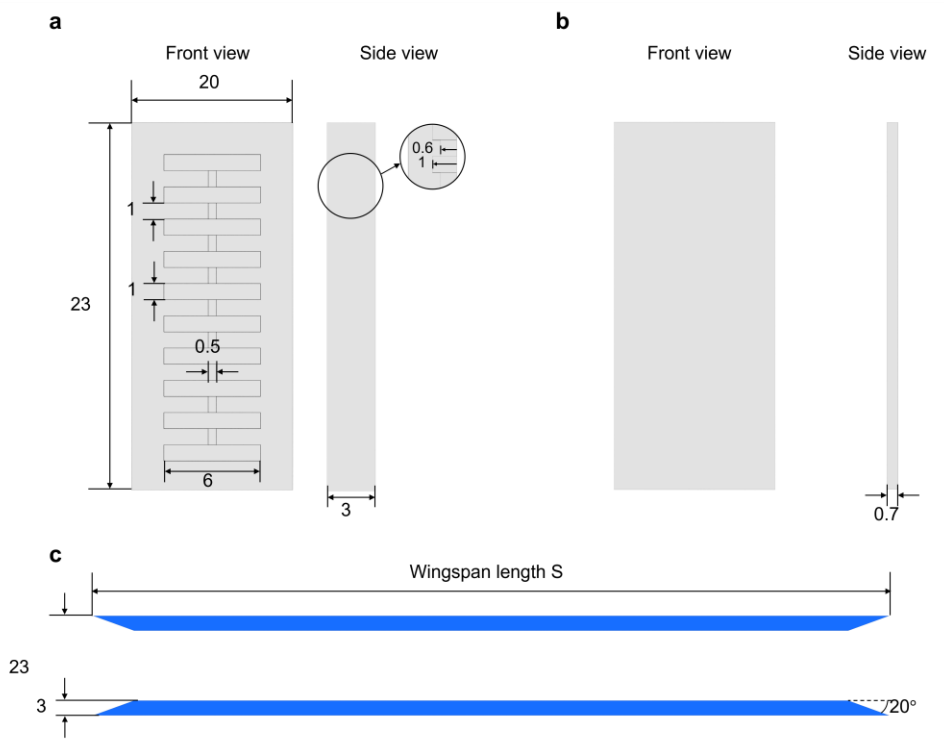

Fig. S3. Geometries of the soft bending actuator and polyester ribbons. (a) Elastomeric channel layer. (b) Elastomeric middle layer. (c) Polyester ribbons.

Thermal oven

Wingspan length	150 mm	155 mm	157 mm	160 mm	170 mm	180 mm
Critical thermal treatment time	43.5 ~ 55.5 min	35 ~ 43 min	21 ~ 29 min	15 ~ 21 min	10 ~ 15 min	6 ~ 10 min

Fig. S4. Thermal treatment. Left shows the oven for thermal treatment. Right shows the table listing required minimum thermal treatment time for transforming from a bistable wing to a monostable wing from.

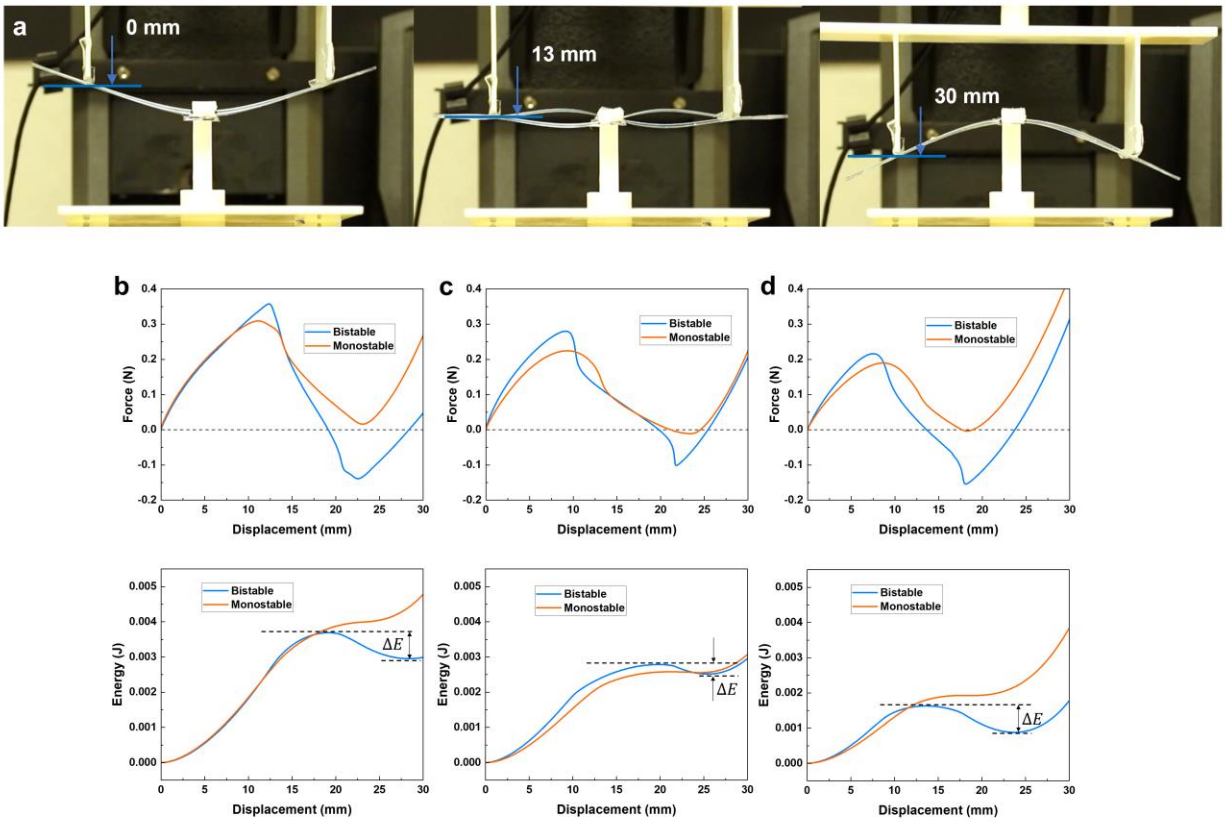

Fig. S5. Force-displacement (*F-d*) and energy-displacement (*U-d*) curves of the flapping wings. (a) Images of displacement-control measurements. (b)-(d) *F-d* (top) and *U-d* (bottom) curves of the wings with wingspan lengths of 160 mm (b), 170 mm (c), and 180 mm (d), respectively.

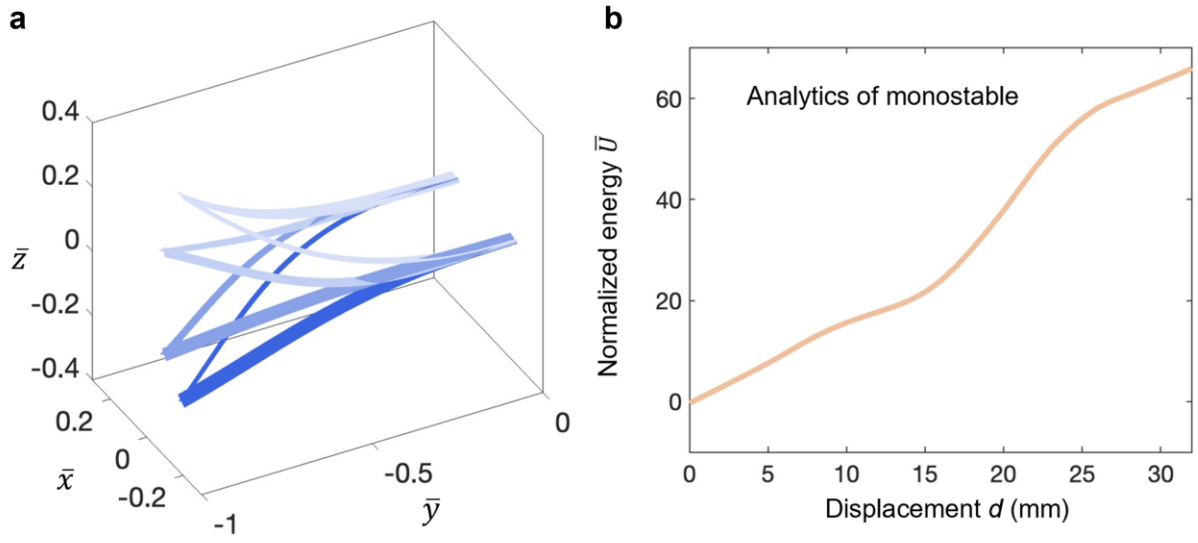

Fig. S6. Results of the analytical model. (a) The monostable deformation process of the wing shape. (b) The corresponding energy variation of the monostable wing.

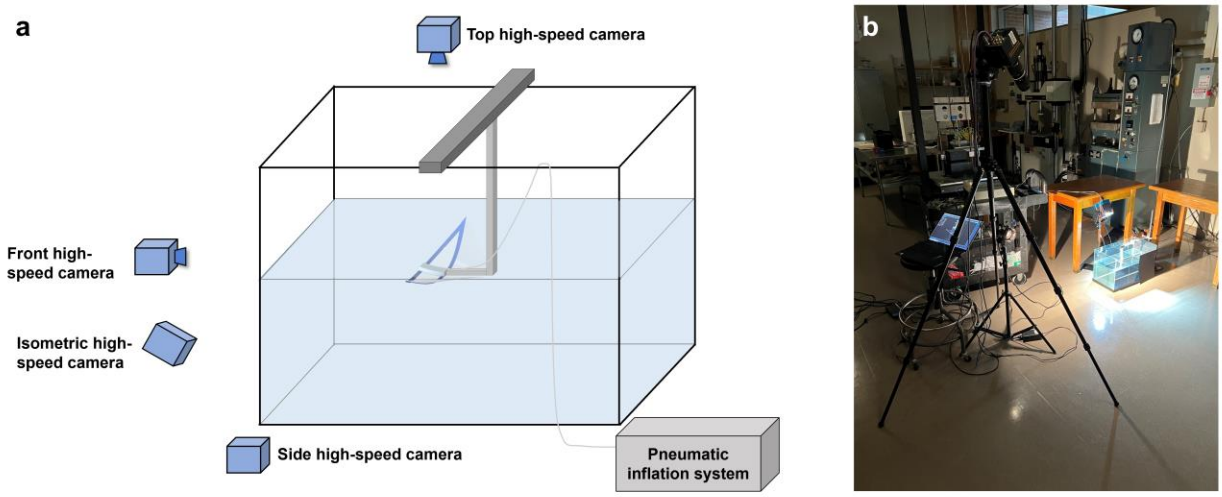

Fig. S7. Experimental setup of high-speed capture. (a) Schematic. (b) Optical image.

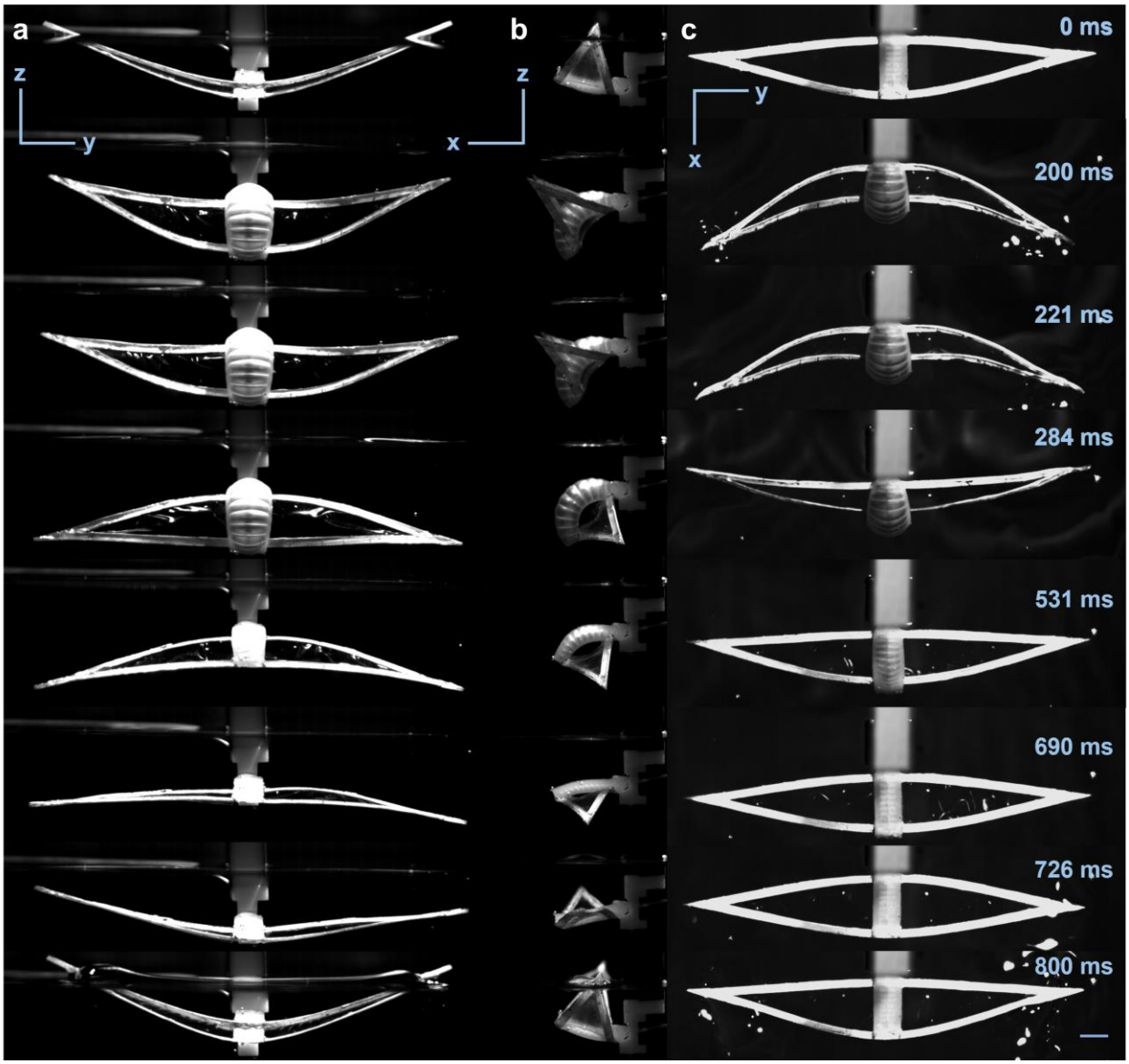

Fig. S8. Time-lapse images of one cycle of the flapping motion. (a-c) Pneumatically actuated flapping motions during a representative cycle of downstroke and upstroke wing flapping, captured in front view (a, left, YZ plane), side view (b, middle, XZ plane), and top view (c, right, XY plane) using three high-speed cameras. Wingspan length: 160 mm. Scale bar: 10 mm.

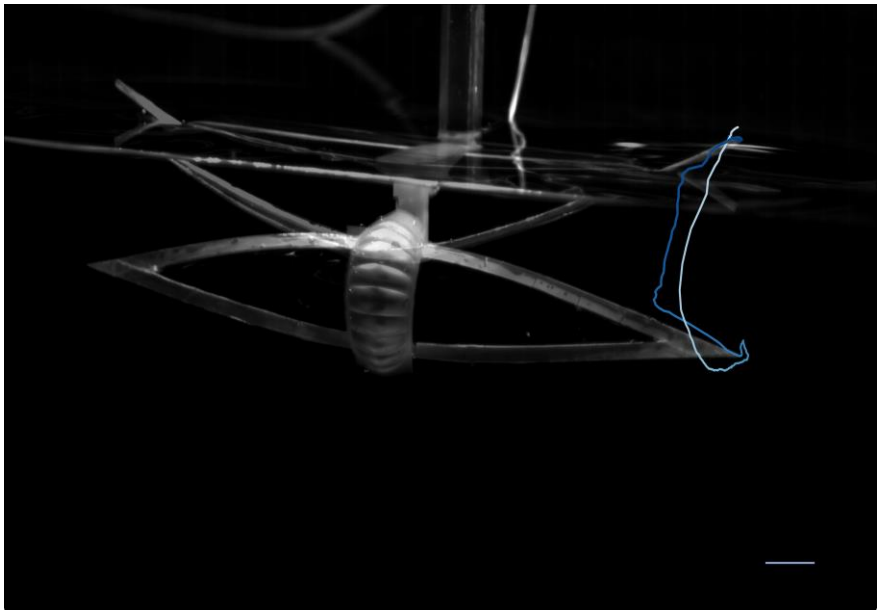

Fig. S9. 3D trajectory of the wing tip of the soft flapping swimmer (stationary) during one cycle of downstroke and upstroke. Scale bar: 10 mm.

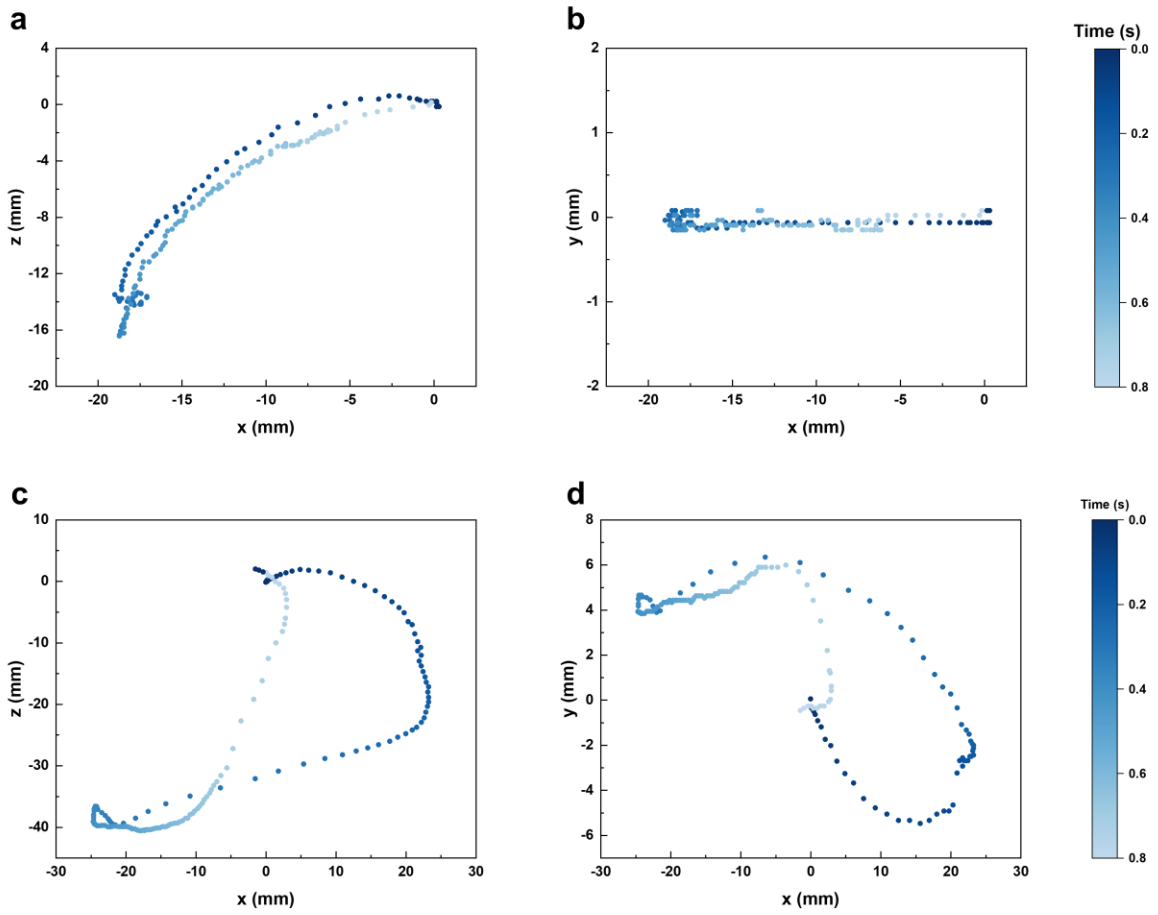

Fig. S10. Trajectory of head and wing tip of the soft flapping swimmer at XZ and XY planes in Fig. S8. (a) Trajectory of the head in XZ plane. (b) Trajectory of the head in XY plane. (c) Trajectory of the wing tip in XZ plane. (d) Trajectory of the wing tip in XY plane.

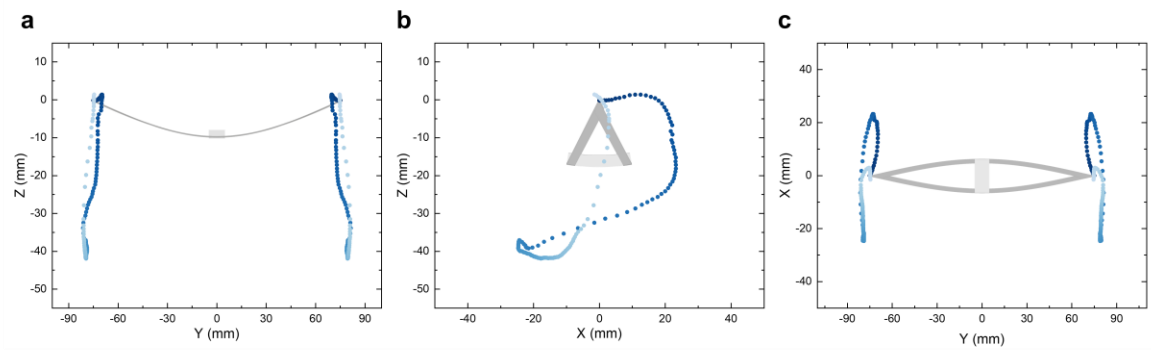

Fig. S11. The trajectory of two wing tips at YZ, XZ, and YX planes. (a) YZ plane. (b) XZ plane. (c) XY plane.

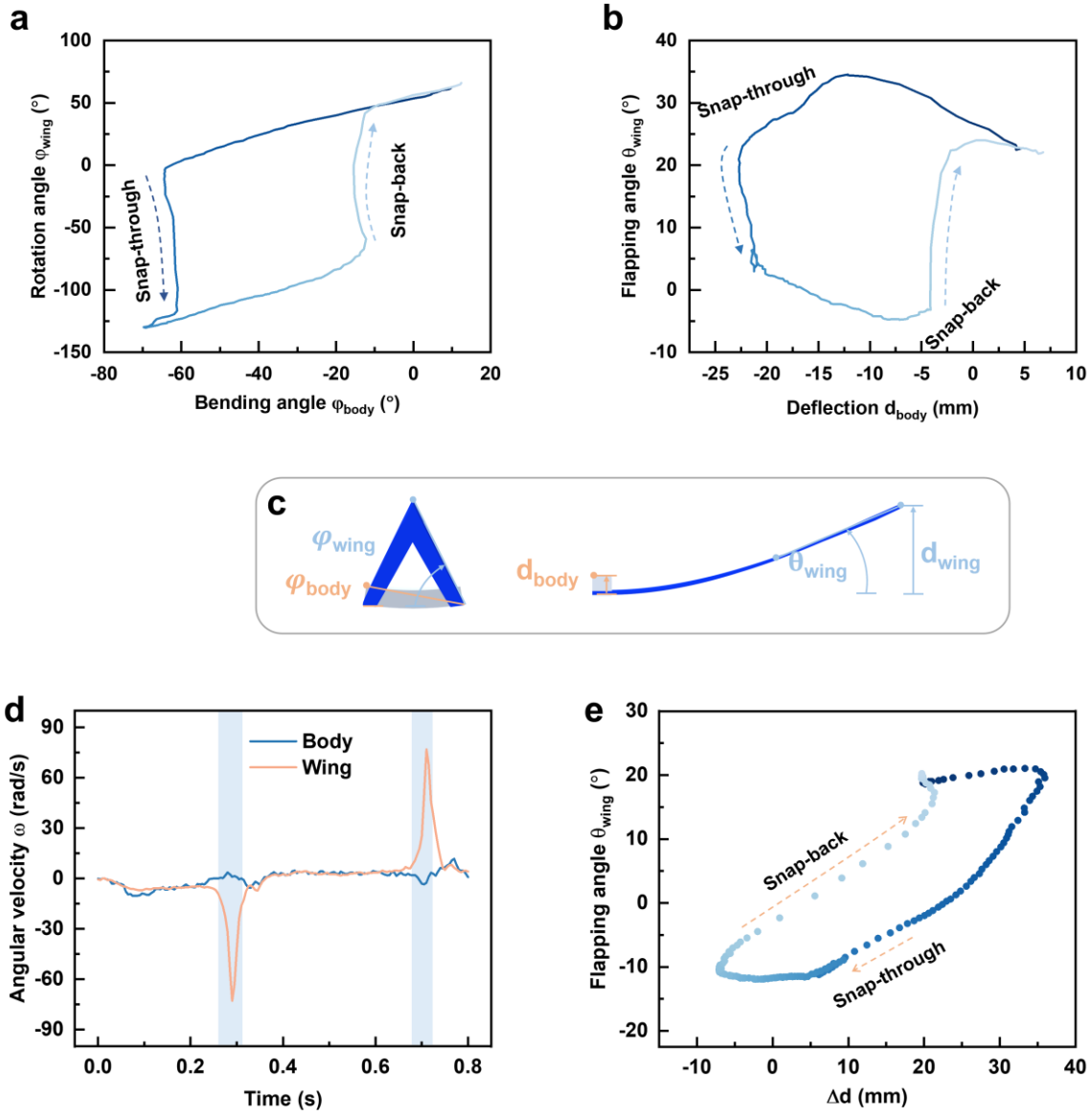

Fig. S12. Flapping and rotation motions in the monostable soft flapping swimmer. (a) Wing rotation angle φ_{wing} as a function of the body bending angle φ_{body}. (b) Wing flapping angle θ_{wing} as a function of body deflection d_{body}. (c) Definitions of soft body bending angle φ_{body} and wing rotating angle φ_{wing} (left), wing deflection d_{wing} and flapping angle θ_{wing}, and soft body deflection d_{body} (right). (d) Angular velocity of body and wing tip as a function of time. (e) Flapping angle θ_{wing} as a function of the difference value of the deflection of body and wing tip Δd. Wingspan length: 160 mm.

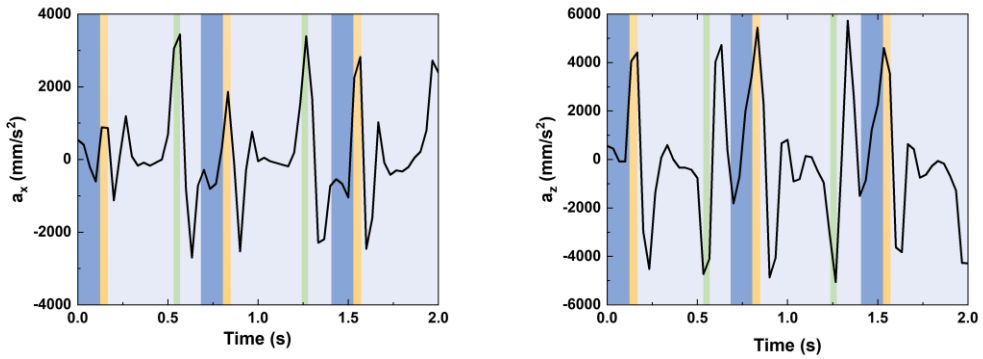

Fig. S13. Corresponding accelerations along the horizontal (x-axis, left) and vertical directions (z-axis, right).

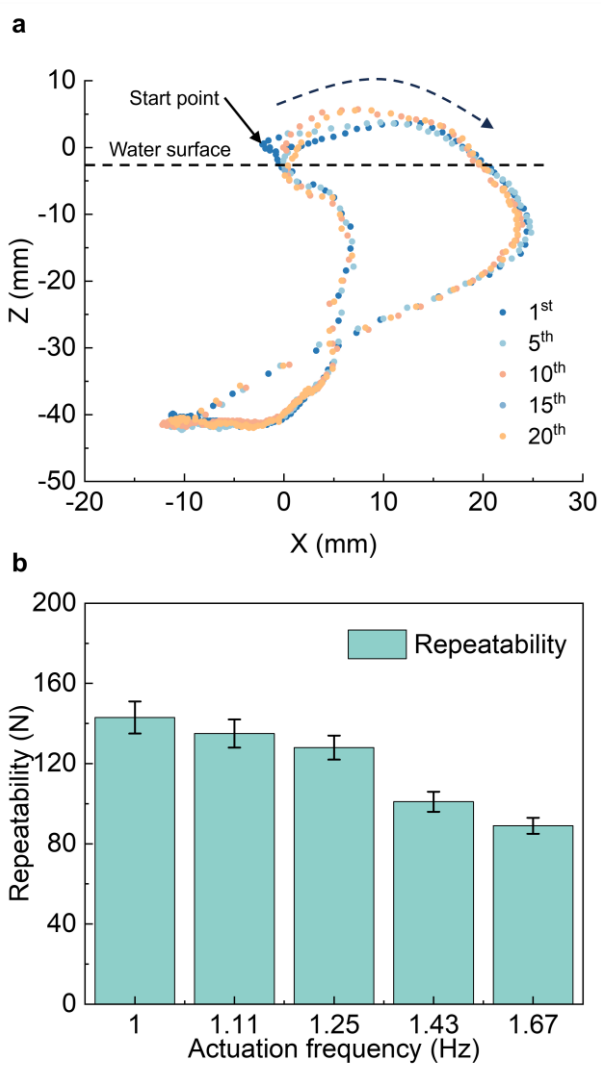

Fig. S14. Repeatability of the flapping motion. (a) Twenty cycles of tracked asymmetric 8-like flapping motion of the monostable wing tip (S = 160 mm) in the XZ plane, actuated at 1.25 Hz. (b) Repeatability N of the flapping motion (S = 160 mm) when actuated at different actuation frequency ranging from 1 Hz to 1.67 Hz.

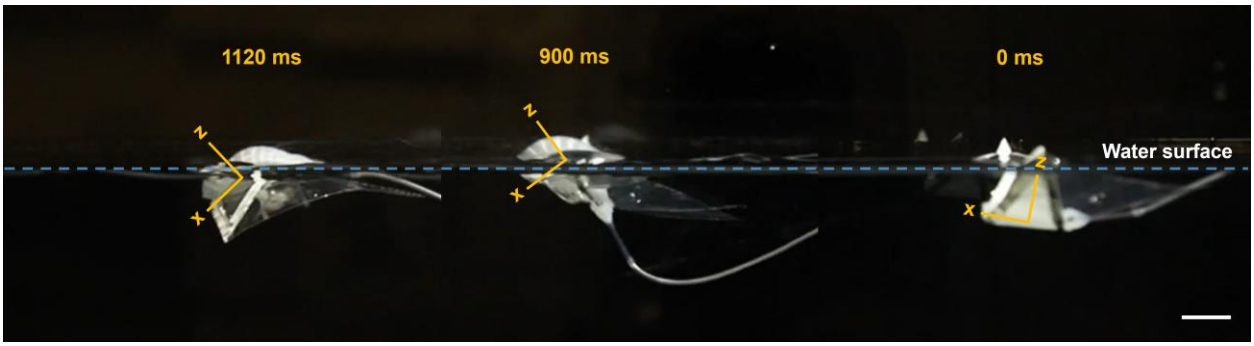

Fig. S15. The definition of angle of attack. Scale bar: 10 mm.

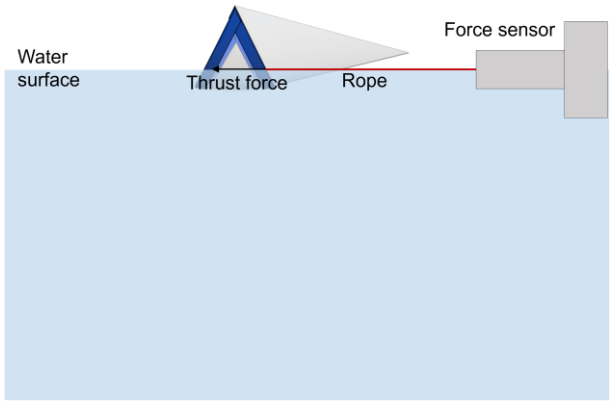

Fig. S16. Schematic illustration of measurement of thrust force.

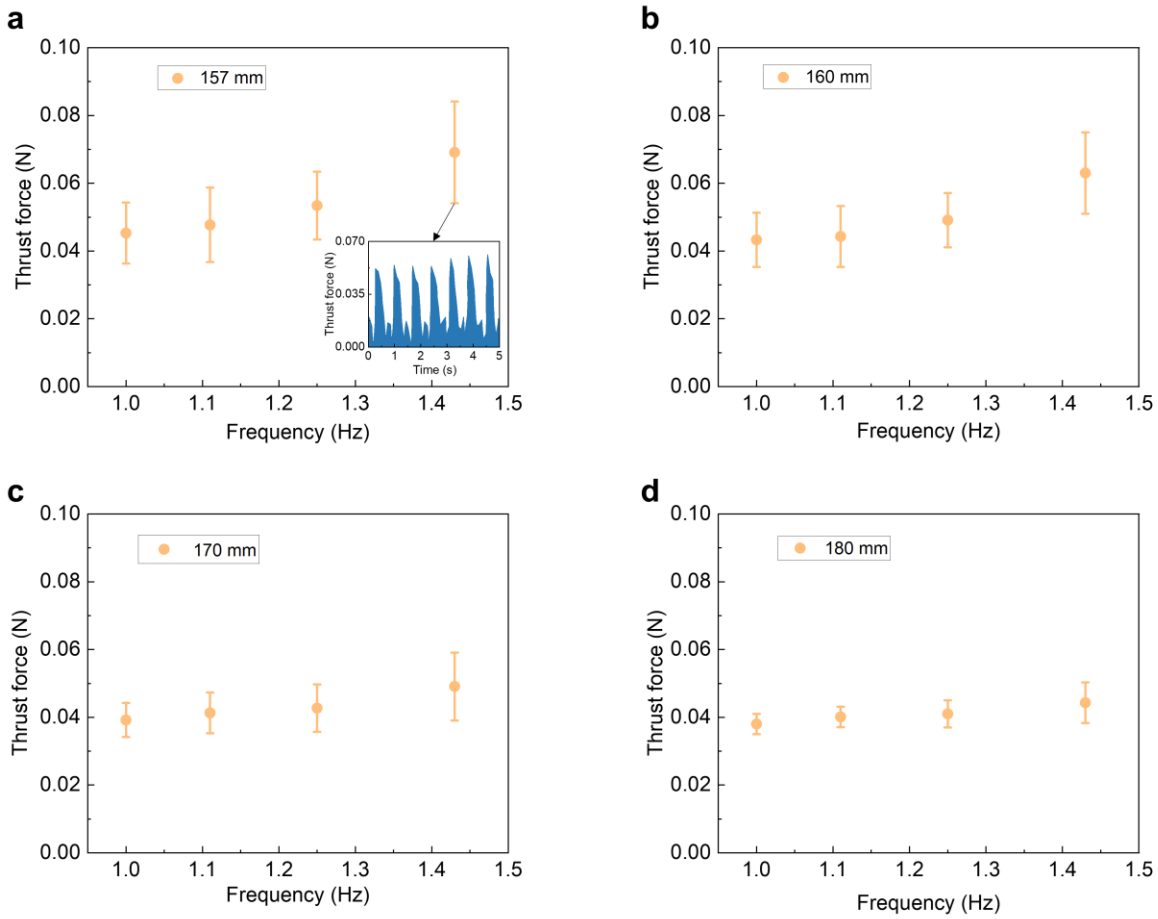

Fig. S17. The thrust force of different wingspan length as a function of frequency. (a)-(d) Different wingspan length S =157 mm (a); 160 mm (b); 170 mm (c); 180 mm (d).

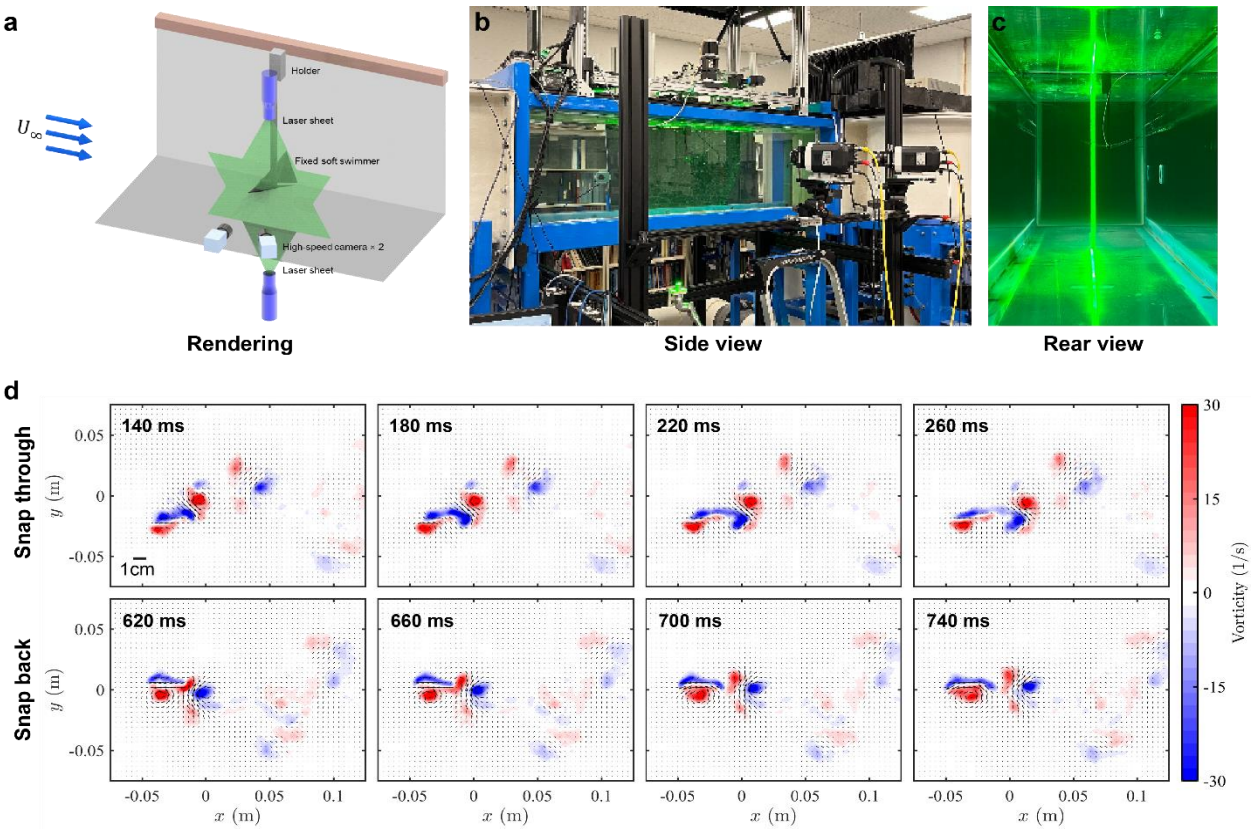

Fig. S18. Planar particle image velocimetry test. (a) A rendering of the experimental setup; (b-c) Side view and rear view of the physical setup; (d) Vorticity fields before and after the snap through (around 220 ms) and snap back (around 700 ms).

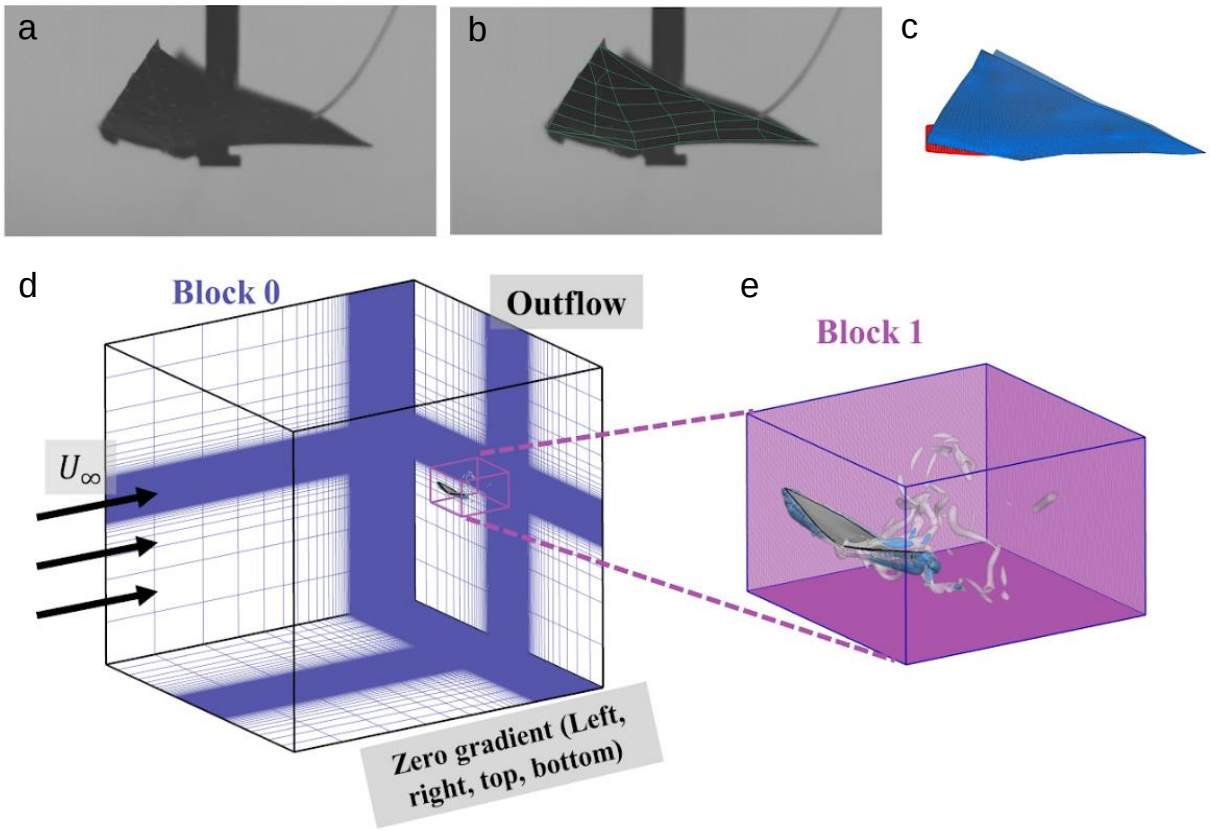

Figure S19. Setup of computational fluid dynamics simulation. (a-c) The reconstruction of body morphology and kinematics for flow simulation, showing (a) video recording of the experiment, with the specimen surface marked with dots, (b) template surface mesh of the computational model overlaid on the video recording, with the nodes of the surface mesh corresponding to the locations of marker points in the video and (c) the smoothed, subdivided and triangulated computational model used in the simulation. (d-e) The computational domain and spatial discretization for the flow simulation, with boundary conditions labeled in (d) the base domain, with the boundary of the nested local mesh refinement block (block 1). A zoomed-in view of the block 1 with the immersed model and the wake formation is shown in (e).

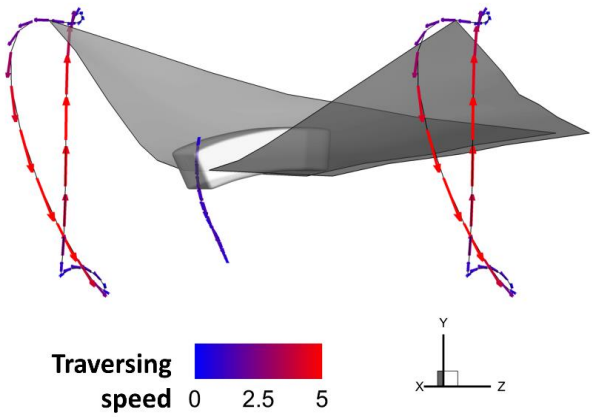

Figure S20. The trajectory of the wing tip and head of the soft swimmer during one stroke of snapping captured from flow simulation.

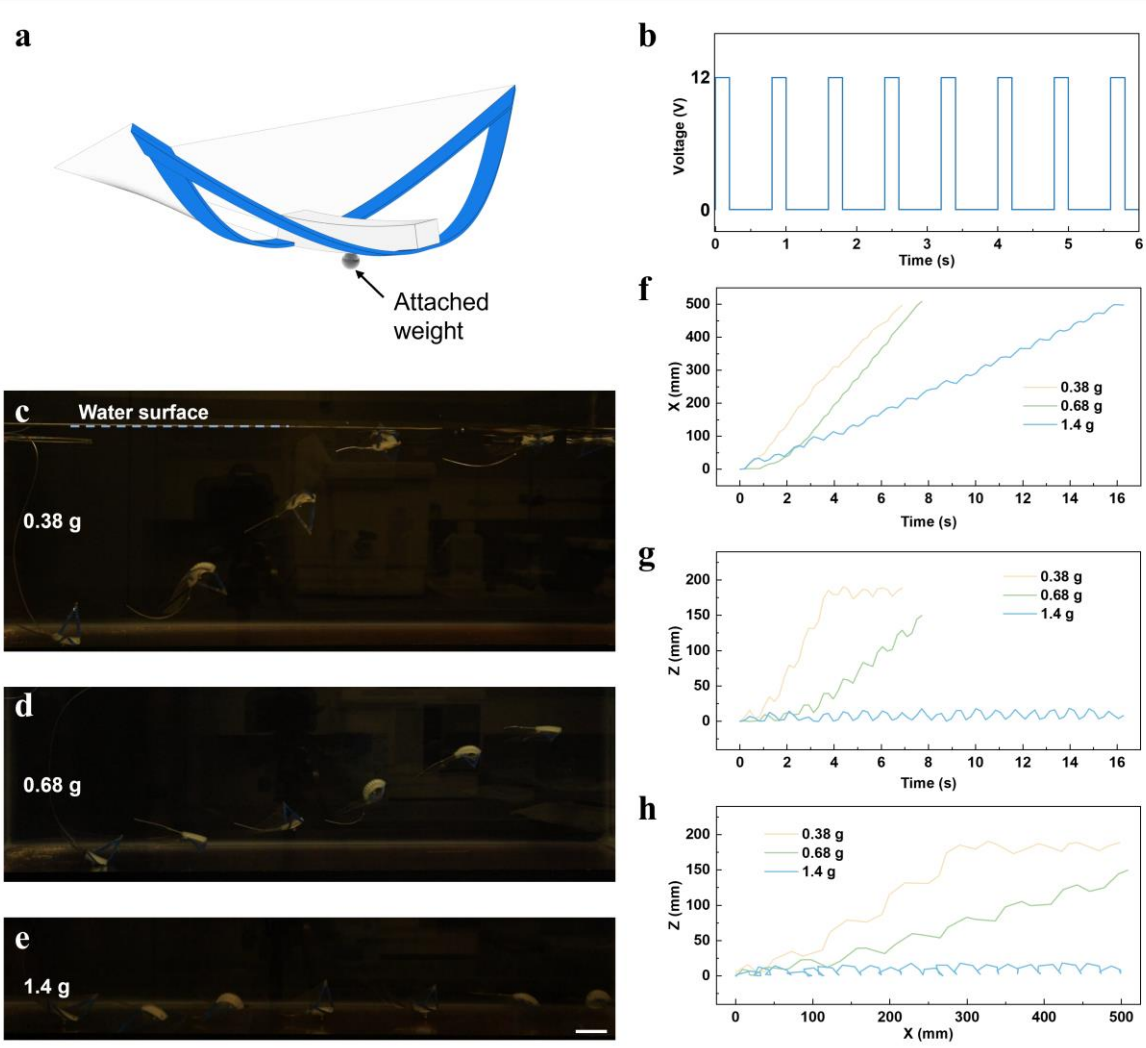

Fig. S21. Underwater swimming behaviors of soft flapping swimmers with different attached weights. (a) Schematics of soft flapping swimmer with the attached weight. (b) The analog control scheme for the output driving signal from the control circuit. (c)-(e) The overlapping time-lapse images of swimming behaviors for soft flapping swimmers with different attached sphere weights under the same actuation frequency of f = 1.25 Hz. (f) The corresponding swimming displacement (in the X direction) over time in (c)-(e). (g) The corresponding swimming displacement (in the Z direction) over time in (c)-(e). (h) The corresponding swimming trajectories in the XY plane in (c)-(e). Scale bar: 20 mm.

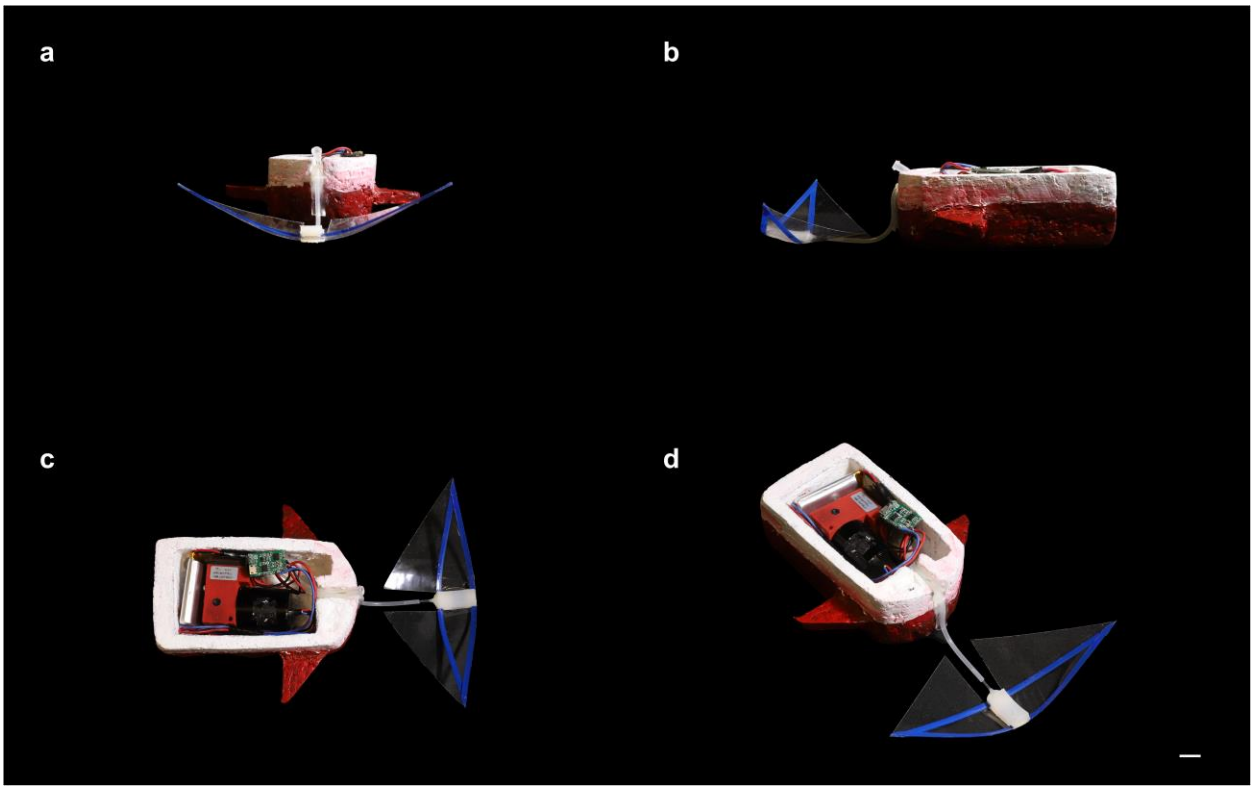

Fig. S22. Configuration of untethered soft flapping swimmer. (a) Front view. (b) Side view. (c) Top view. (d) Isometric view. Scale bar: 10 mm.

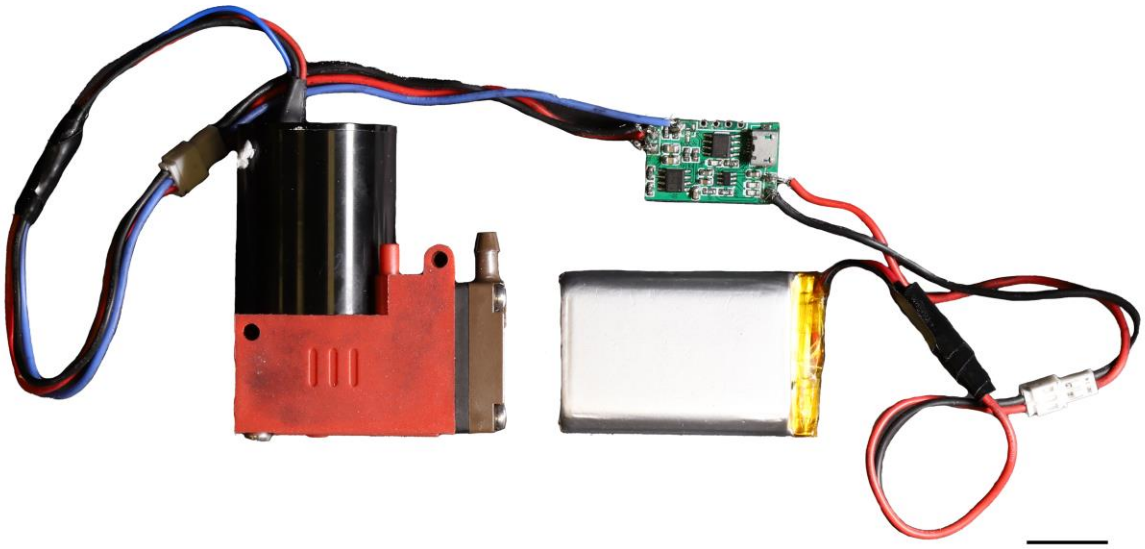

Fig. S23. Connecting form of the air pump, circuit board, and battery. Scale bar: 10 mm.

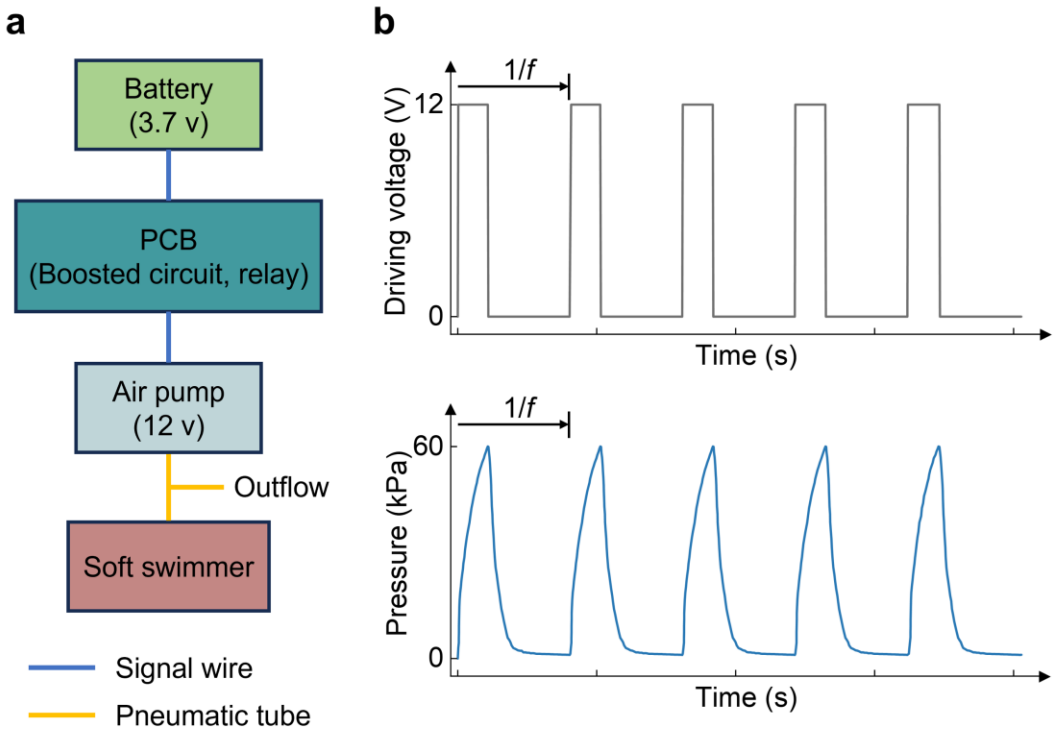

Figure S24. Untethered actuation system for soft swimmers. (a) Diagram of the untethered actuation system. (b) The control signals, including driving voltage and air pressure.

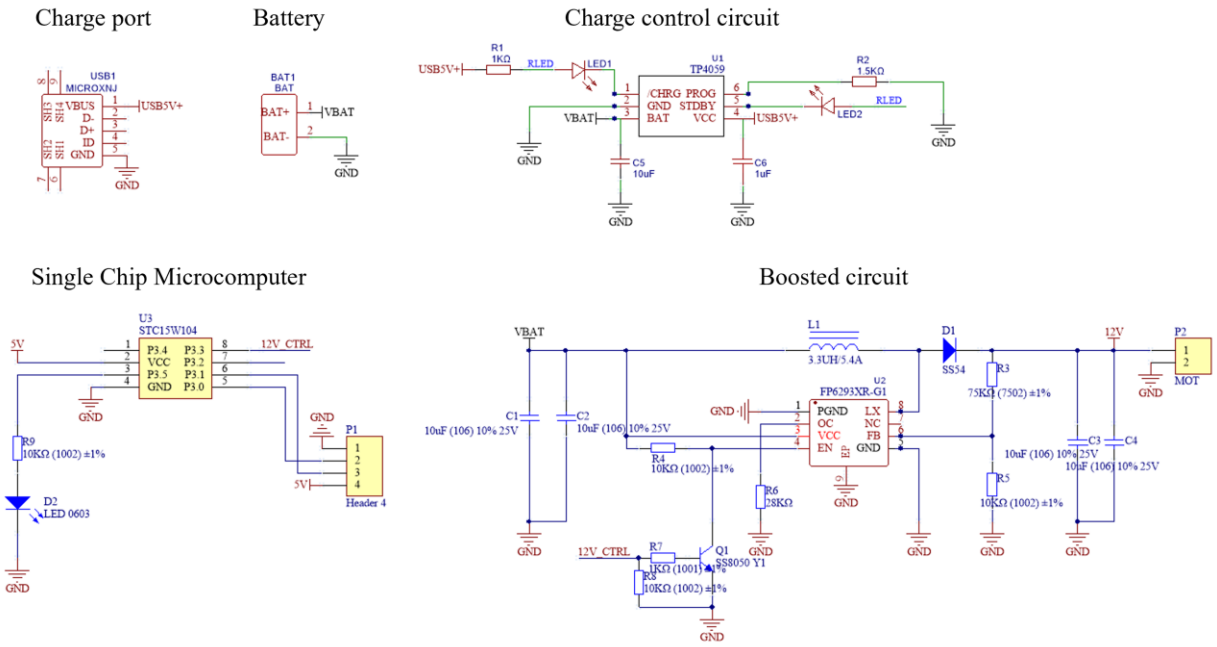

Fig. S25. Schematic diagram of all parts in circuit board.

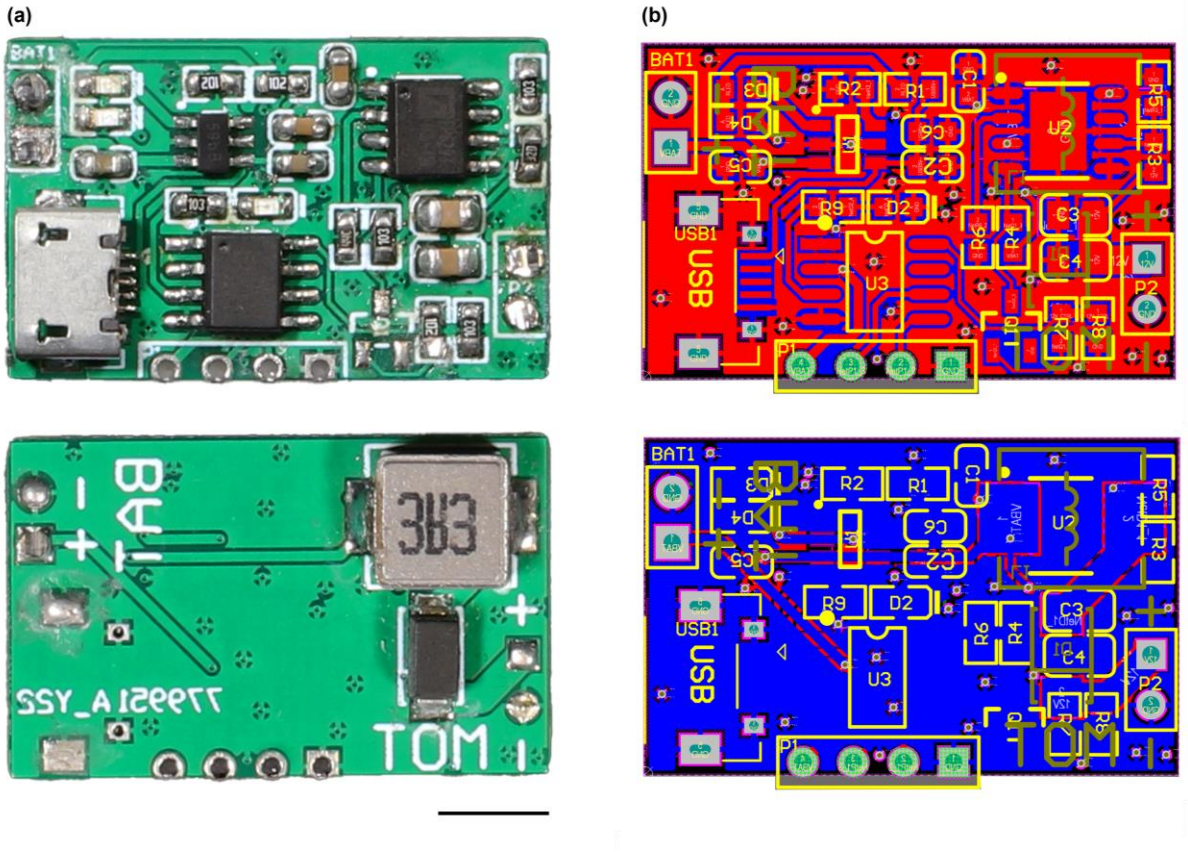

Fig. S26. Circuit board. (a) Front and back optical images of circuit board; (b) Board layout with indicated traces and footprints. Scale bar: 4 mm.

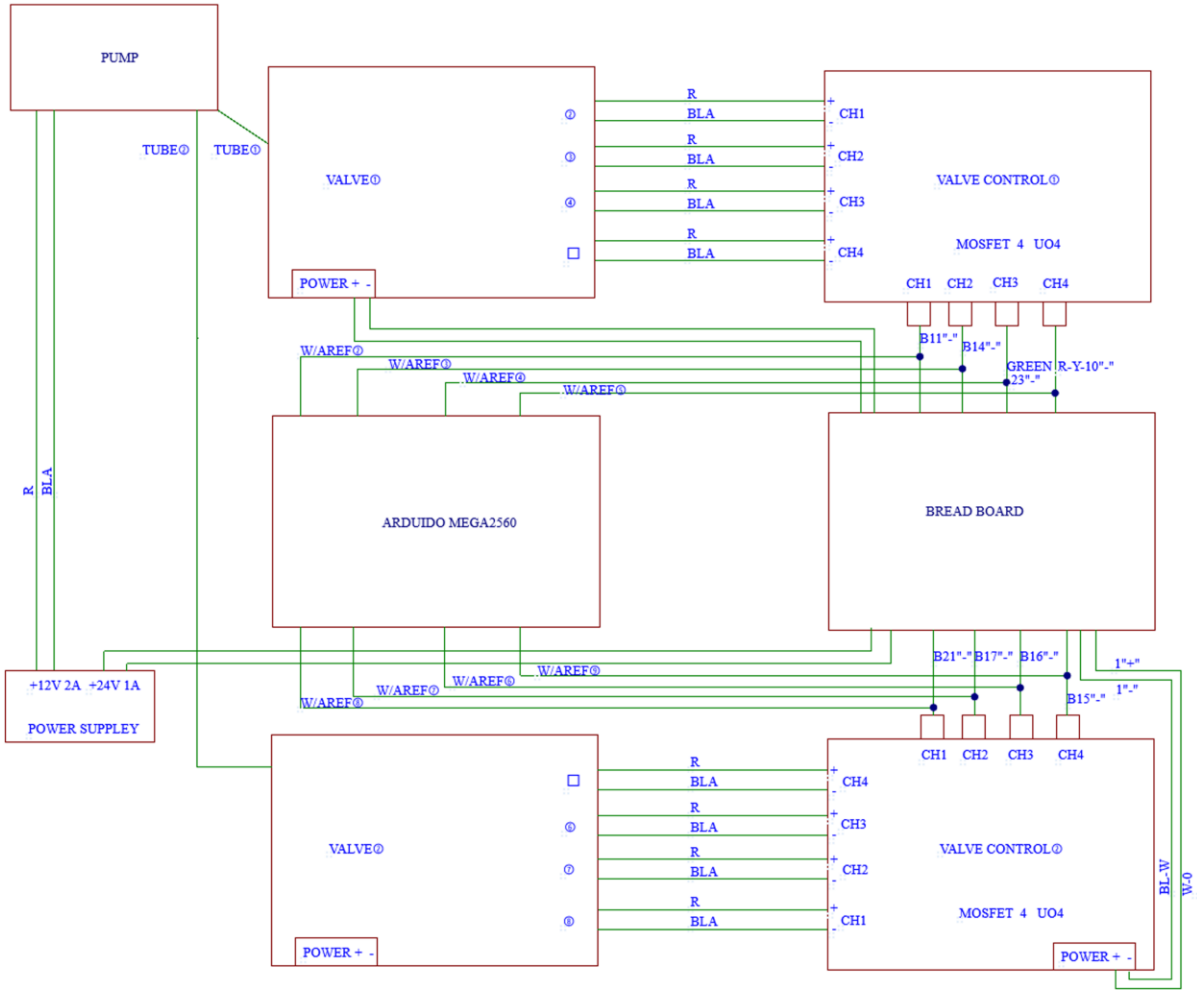

Fig. S27. Schematic diagram of all parts of the air pump setup.

Table S1. Comparison this work with the bistable soft swimmer.

	Max. speed (BL/s)	Min. CoT	Weight (g)	Max. frequency (Hz)	0.2 < St < 0.4	Snapping behavior	Actuation
This work	**6.8**	**23.7**	2.2	**1.67**	√	Monostable	**Single input**
Bistable soft swimmer [14]	3.74	39	**3.1**	1	√	Bistable	Double inputs

	Waveform	Swimming behavior	Maneuverability (Depth)	Load carrying capability	Untethered design
This work	**Square**	Air-water interface; **underwater**	**High**	√	√
Bistable soft swimmer *(14)*	sinusoidal	Air-water interface only	N.A.	N.A.	×

Table S2. Comparison this work (tethered version) with the other tethered soft swimmers based on maximum speed.

Category		Max. speed (BL/s)	Body length (mm)	Max. speed (mm/s)	Weight (g)	Frequency (Hz)	Actuation	Ref.
Tethered soft swimmer	Soft electronic fish	1.45	93	135	42.5	5	Electric	*(8)*
	Bistable soft swimmer	3.74	22.8	85.27	3.1	1	Pneumatic	*(14)*
	Tunabot	4	255	1020	306	15	Electric	*(25)*
	Resonant squid-inspired robot	0.98	266	260	380	9	Electric	*(26)*
	Soft Biomimetic Fish Robot	0.25	150	37.2	4.4	0.75	Electric	*(27)*
	Spine-inspired soft robot	0.78	150	117	51	1.3	Pneumatic	*(28)*
	This work	**6.8**	**23**	**156.4**	**2.2**	**1.67**	**Pneumatic**	

Table S3. Comparison this work (untethered version) with the other untethered soft swimmers based on maximum speed.

Category		Max. speed (BL/s)	Body length (mm)	Max. speed (mm/s)	Weight (g)	Frequency (Hz)	Actuation	Ref.
Untethered soft swimmer	Soft-robotic ray	0.196	16.3	3.2	0.011	1.5/3	phototactic	*(2)*
	Swimming biohybrid fish	1.07	14	15	0.025	3.6	phototactic	*(3)*
	Soft electronic fish	0.69	93	64	90.3	5	Electric	*(8)*
	SoFi	0.51	470	239.7	1600	1.15	Pneumatic	*(19)*
	Flapping Insect-scale soft aquabot	1.02	19.5	19.89	1.47	1	Electroosmotic hydrogel	*(31)*
	Sculling Insect-scale soft aquabot	0.53	35	18.55	2.51	0.33	Electroosmotic hydrogel	*(31)*
	This work	**1.18**	**30**	**35.4**	**4.4**	**0.77**	**Pneumatic**	

Table S4. Comparison this work with swimming animals based on maximum speed.

Category	Max. speed (BL/s)	Body length (m)	Max. speed (m/s)	Weight (kg)	Ref.
Clearnose skate (*R. eglanteria*)	2.25	0.79	1.78	1	*(6)*
Stingray (*D. sabina*)	2.5	0.21	0.53	9	*(6)*
Salmon (*Salmo salar L.*)	6.4	0.55	3.52	5	*(33)*
Pike (*Esox lucius*)	10.45	0.38	3.97	15	*(34)*
Leopard shark (*T. semifasciata*)	1.6	0.5	0.8	20	*(35)*
Blue whale (*B. musculus*)	0.4	25	10	5000	*(36)*
Killer whale (*Orcinus orca*)	1.88	8.2	15.4	7500	*(37)*
Dolphin (*D. delphis*)	4.38	1.83	8	104.8	*(38)*

Supplementary movies

Movie S1. Free surface swimming behavior of the soft flapping swimmer.

Movie S2. Stationary swimming behavior of the soft flapping swimmer.

Movie S3. Free-surface swimming performance actuated with different frequencies.

Movie S4. Particle image velocimetry tests (quarter-span).

Movie S5. Vorticity field is at the quarter-span (particle image velocimetry).

Movie S6. Vorticity field at the quarter-span (computational fluid dynamics).

Movie S7. 3D wake formations (computational fluid dynamics).

Movie S8. Multimodal maneuverable swimming modes of the soft flapping swimmer.

Movie S9. Load-carrying capability during the swimming of the soft flapping swimmer.

Movie S10. Navigation in complex, unstructured underwater environments.

Movie S11. High swimming stability of the soft flapping swimmer when it's subjected to external perturbations.

Movie S12. Untethered swimming of the soft flapping swimmer in an outdoor natural pond.